minerals

MDPI

Article

Airborne/UAV Multisensor Surveys Enhance the Geological Mapping and 3D Model of a Pseudo-Skarn Deposit in Ploumanac'h, French Brittany

Guillaume Martelet [1,*], Eric Gloaguen [1,2], Arne Døssing [3,4], Eduardo Lima Simoes da Silva [3,4], Johannes Linde [5] and Thorkild M. Rasmussen [6]

1 Bureau de Recherches Géologiques et Minières (BRGM), F-45060 Orléans, France; e.gloaguen@brgm.fr
2 ISTO, UMR7327, Université d'Orléans, CNRS, BRGM, F-45071 Orléans, France
3 CMAGTRES, Geomagnetism, DTU Space, Technical University Denmark, Centrifugevej 356, DK-2850 Kgs. Lyngby, Denmark; ards@space.dtu.dk (A.D.); edsd@space.dtu.dk (E.L.S.d.S.)
4 DTU CERE, Technical University Denmark, DK-2850 Kgs. Lyngby, Denmark
5 Geodesy and Earth Observation, DTU Space, Elektrovej 328, DK-2850 Kgs. Lyngby, Denmark; jlinde@space.dtu.dk
6 Department of Civil, Environmental and Natural Resources Engineering, Luleå Technical University, 971 87 Luleå, Sweden; thorkild.maack.rasmussen@ltu.se
* Correspondence: g.martelet@brgm.fr; Tel.: +33-(0)238644732

Abstract: Taking advantage of a multi-sensor (multispectral and magnetic) drone survey, we address the detailed geological mapping and modeling of a mineralization in its geological environment. We stress that these high-resolution data allow us to bridge the gap between field observations and a regional aeromagnetic survey. On the one hand, the combination of multispectral imagery with field geological observations enhances detailed geological mapping. On the other hand, the combination of field magnetic susceptibility measurement and their use in detailed to regional magnetic modeling, constrained respectively by UAV-borne and airborne magnetic surveys, allows deriving a model of the mineralization consistent across the scales. This is demonstrated in a case study in a complex polyphased magmatic-metamorphic environment on the coast of French Brittany. The target area hosts a pseudo-skarn mineralization, exhibiting an outstanding magnetic anomaly. The combination of remotely sensed and field data allows deriving a realistic conceptual and geometrical model of the magnetic mineralization in its geological environment, tightly constrained by field observations and measurements.

Keywords: pseudo-skarn; airborne geophysics; magnetic modelling; drone; UAV; multispectral image; multiscale

Citation: Martelet, G.; Gloaguen, E.; Døssing, A.; Lima Simoes da Silva, E.; Linde, J.; Rasmussen, T.M. Airborne/UAV Multisensor Surveys Enhance the Geological Mapping and 3D Model of a Pseudo-Skarn Deposit in Ploumanac'h, French Brittany. *Minerals* **2021**, *11*, 1259. https://doi.org/10.3390/min11111259

Academic Editor: Yosoon Choi

Received: 5 October 2021
Accepted: 8 November 2021
Published: 12 November 2021

1. Introduction

In the last decade, UAV-borne geophysics has undergone rapid developments (e.g., [1]). Several sensors (geophysical methods such as magnetics, radar, VLF, radiometrics) are now surveyed, in R&D to operational mode, and developments are in fast progress in all parts of the world (e.g., [2,3]), including for emerging methods such as electromagnetism or gravity [4,5]. This is often driven by applications, which are as diverse as agriculture (e.g., [6]), ground water (e.g., [7]), oil and gas (e.g., [8]), UXO, or mine detection (e.g., [9]). The mining sector is no exception to this craze: this new way to quickly recover small to medium extent high-resolution data is being integrated into the companies' toolbox (e.g., [10]). Accordingly, higher resolution on buried structures is gained from the dense information and proximal detection achieved with UAV. The UAV-borne geophysical survey also bridges the gap between field observations/measurements and more regional data such as traditional airborne geophysics (e.g., [11]). This is one of the key points that we address in this paper: drone surveys provide data at a scale perfectly compatible with field

observations allowing a mutual field/drone enhancement in the interpretation process. Also, interpretations/models can be confronted to geophysical data acquired at different scales (for instance drone and regional airborne): this both strengthens and refines the geological interpretations.

We demonstrate this mutual enforcement of geology and geophysical data across the scales, from the field to the regional airborne scale, through a case study focused on a mineralized area (a few hundred meters in extent), located on the coast of French Brittany in the vicinity of Ploumanac'h city (Figure 1). This mineralized pseudo-skarn (the meaning of the pseudo-skarn term will be explicit hereafter) occurrence has been known for a long time (e.g., [12]), because it displays a bright and focused magnetic anomaly cross-cutting well-exposed terrains outcropping along the rocky coast. Because this mineralized occurrence has very little industrial potential (Ploumanac'h is a touristic hot spot, and the magnetic anomaly is mostly developed in the sea), it has never been specifically explored in geophysics. Therefore, as a methodological demonstrator, in the framework of the Muverdrone EIT-RM project, we conducted a multi-sensor UAV survey within the bright regional magnetic anomaly, along the coast—including multispectral, gamma-ray, and magnetic measurements, together with detailed field observations and measurements. In this paper we focus on the combination of field observations and measurements (magnetic susceptibility) with magnetic data. Modeling of magnetic data is performed at two scales using the drone-based survey and a regional airborne survey; finally, a 3D model consistently integrates all the structural and geophysical information. It is shown that the mutual enhancement of the magnetic information at the two scales, tightly constrained by field evidence, allows achieving a consistent geometric and conceptual model of the mineralization in its geological environment.

Figure 1. The study area along the coast, between the cities of Ploumanac'h and Perros-Guirec, at intermediate-low tide (view towards the SE).

2. Materials and Methods

2.1. Geological Context

The study area (Figure 2) is located in a remnant of the Neoproterozoic Panafrican orogeny, partly preserved from the Variscan orogeny, which largely overprints Panafrican terranes elsewhere in Europe. In this area, the Panafrican orogeny corresponds to the Cadomian belt, which constitutes the northern part of the Armorican massif. This Cadomian belt also includes Paleo-Proterozoic remnants that extend from the Morlaix bay in the southwest up to northern Normandy, through the Anglo-Normand islands in the English Channel. This Paleo-Proterozoic basement, called Icartian (from the Icart Point, Guernesey island), composed of volcano-sediments, is only observed in the Cadomian Trégor Unit where it constitutes the basement of Neoproterozoic sediments [13]. In the northern part of

the Trégor Unit, this Paleo-Proterozoic basement is intruded by the North-Trégor plutonic-volcanic complex, dated at 615 ± 7 My (U/Pb on zircon, [14]), made of granites and their volcanic equivalents ([15] and references therein). This felsic complex is crosscut by several generations of SW-NE-trending and SE-NW-trending mafic dykes. Two generations of the mafic dyke swarm are imprecisely dated at 440 and 350 My (K/Ar whole rock, [16]). The latter could correspond to a ca. 360–350 My large mafic event represented by the neighboring Saint-Jean-du-Doigt gabbro intrusion in the Morlaix bay [17] and a regional swarm of dolerite dykes [18]. Finally, the late-Variscan Ploumanac'h igneous complex made of monzogranite, syenogranite, gabbro, and granites intrude the area crosscutting all the previous lithologies. The first intrusion of this complex is dated at 302 ± 15 My (Rb/Sr whole rock, [19]) and 295 ± 3 My (U/Pb zircon, in [20]) and is cogenetic of gabbro intrusion [21]. The syenogranite and the monzogranite that constitute the border of the complex are characterized by a high content of thorium and uranium (up to 94 and 48 ppm respectively [22], mainly hosted by allanite and zircon [23]. The amount of hornblende and biotite as well as the presence of molybdenite-bearing pegmatites and orbicular facies [24], underline the water enrichment of the initial melt. Metasomatic replacement between mafic dykes and the Cadomian Perros-Guirec granite by hydrothermal fluids associated to the Variscan Ploumanac'h granite form skarn-*like* masses along geological contacts [12]. Indeed, these pseudo-skarns are composed of garnet (grossular-andradite), magnetite, epidote, albite, quartz, pyrite, molybdenite, and scheelite [12].

2.2. Data Acquisition

2.2.1. Multispectral UAV Data

A drone-borne high-resolution multispectral survey was achieved in October 2019, in two flights/blocks, with a MicaSense RedEdge-M camera, fitted by DTU on a multirotor DJI M210 drone. Individual scenes were acquired as 1.23 Mpixels (1280 × 960) rasters, coded on 16 bits, including georeferencing. The flight was performed at a constant altitude of 80 m a.m.s.l. and a constant speed of 6 m/s. Survey lines were flown roughly parallel to the coast at a 20 m spacing. More than 800 scenes were mosaicked, georeferenced, and orthorectified on each survey block, using Pix4Dmapper software. Final products include a DTM and mesh of the surface, as well as a 3-band mosaic with a pixel size of 5 cm. An extract of the southern block mosaic is displayed in Figure 3, together with the detailed geological contours.

2.2.2. Airborne Magnetic Data (Fixed Wing and UAV)

Both regional fixed wing airborne magnetic data and local detailed UAV-borne data are available for this study (Figure 4).

The regional aeromagnetic data derive from a fixed wing airborne magnetic and radiometric survey flown in 1998 all over French Brittany, by Sander Geophysics, for BRGM. The survey was conducted in drape flying mode, 120 m above the topography, using differential GPS and a radar altimeter. In the study area, the flight/tie line spacing is 500/10,000 m. On-board magnetic data were recorded with a Scintrex CS-2 Cesium vapor absolute magnetometer and diurnal magnetic variations were corrected for using a continuous recording of a G822A Geometrics located some tens of kilometers apart from our study area. Detailed survey parameters and processing are reported in [25]. The magnetic anomaly map derived from this survey on our study area is presented in Figure 4.

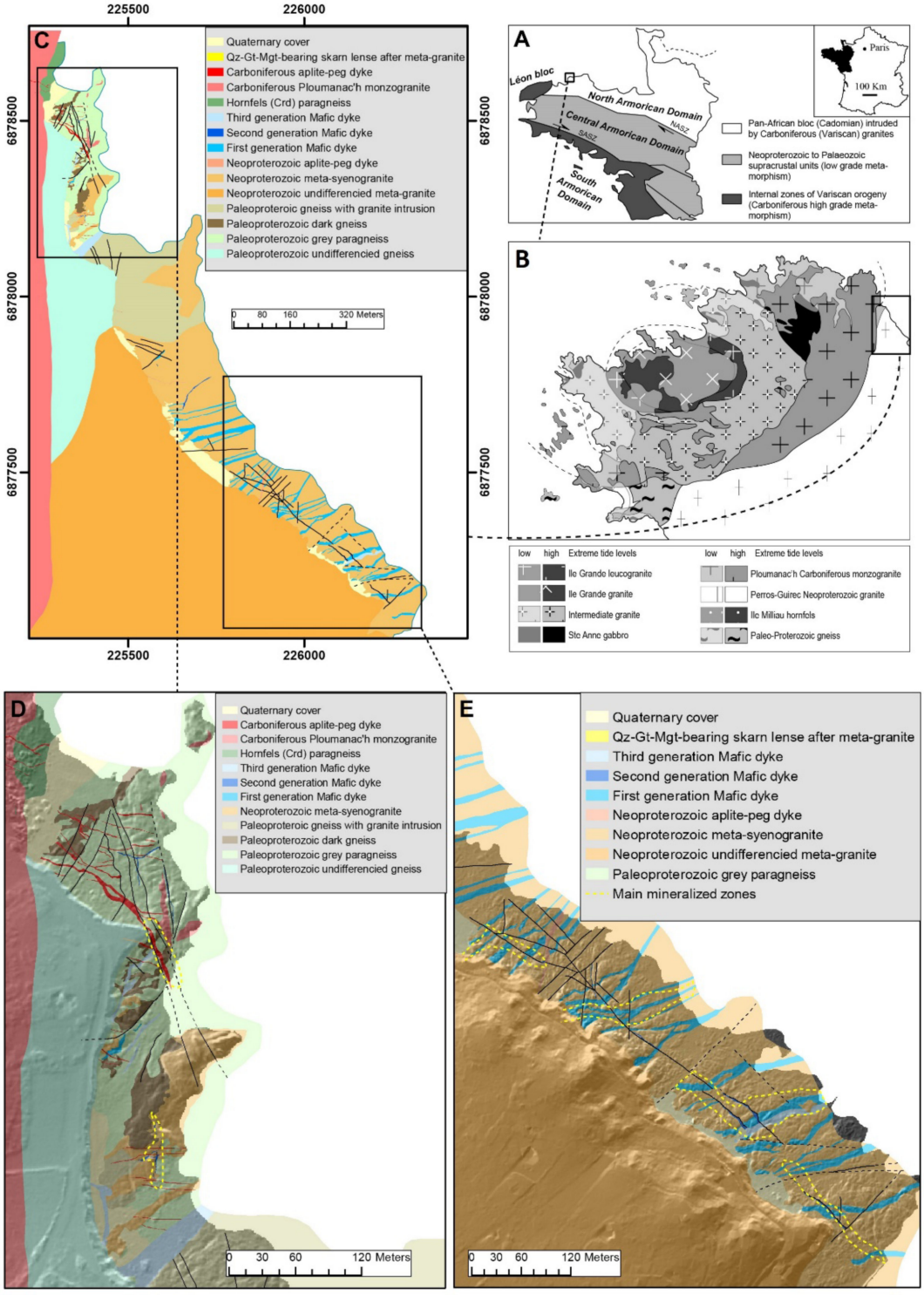

Figure 2. Geological map and location of the study area. (**A**) Sketch map of the Armorican massif displaying the main geological domains and the location of the study area. (**B**) Simplified geological map of the Ploumanac'h igneous complex, modified from [21]; the study area is located on the eastern border of the complex. (**C**) Geological map of the working area (this study). (**D**) Detailed geological map of the Ranolien sector displaying the contact between the Paleo-Proterozoic host, the Neoproterozoic Perros-Guirec granite and the Ploumanac'h Carboniferous granite. Pegmatites and aplite dykes (in red) derived from Ploumanac'h pluton crosscut all the previous lithologies. Sun-shading using 1 m × 1 m resolution RGE ALTI Digital Terrain Model from IGN. (**E**) Detailed geological map of the Trestraou sector showing the high density of mafic dykes crosscutting the Perros-Guirec Neoproterozoic granite. Note that numerous dykes are crosscut by NW-SE faults. Main mineralized zones along NW-SE faults and along mafic dyke contacts are highlighted by yellow-dashed lines.

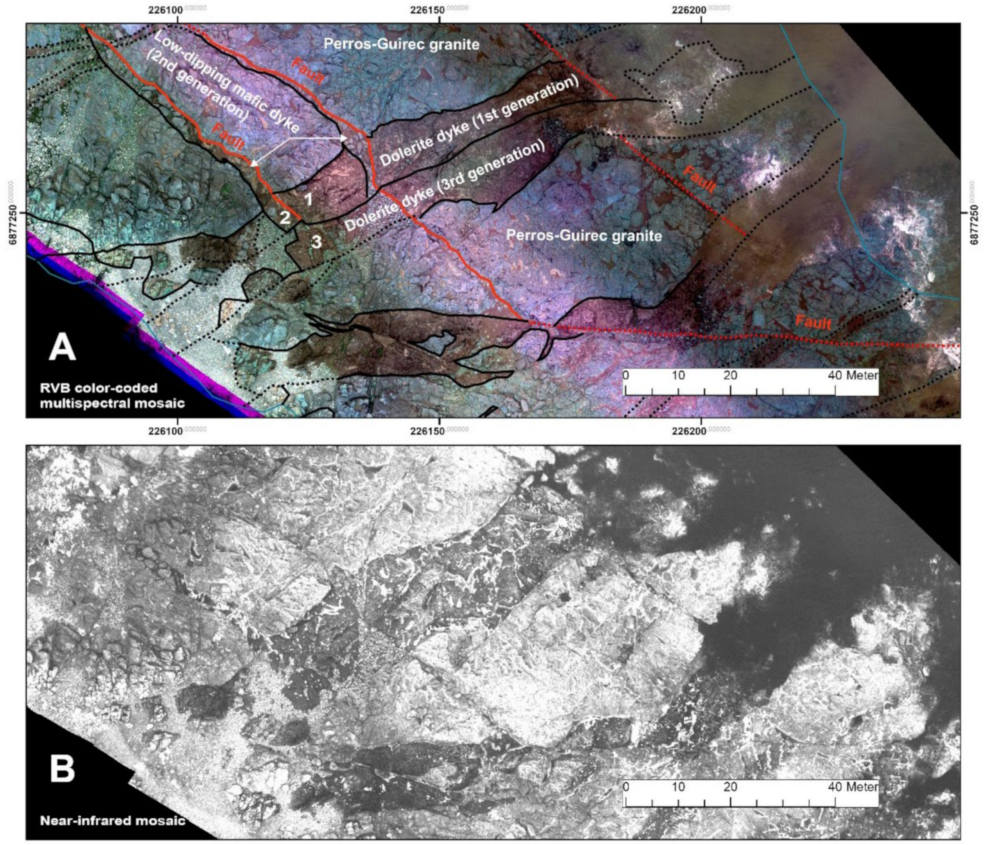

Figure 3. Extracts of (**A**) the RVB color-coded multispectral and (**B**) near-infrared mosaics on a subarea of the southern block (Trestraou sector) surveyed by drone. In (**A**) detailed geological contours (in black) and faults (in red) are superimposed, derived from the joint interpretation of field observations and the mosaics. Relations between the three generations of mafic dykes are highlighted: The first generation NE-SW-trending mafic dyke (dolerite), noted 1, is crosscut by the second generation of NW-SE mafic dyke (noted 2) emplaced within low-dipping reverse faults (in red). 1 and 2 are both crosscut by the third generation (noted 3) of NE-SW-trending mafic dyke (dolerite).

The magnetic UAV-borne data were surveyed in October 2019, in four flights/blocks in less than three hours, with a survey-grade multirotor drone from DTU [26], towing a single Rubidium absolute QuSpin magnetic sensor fitted in a bird. The bird was towed 4.5 m below the UAV, at a constant altitude of 15/30 m a.m.s.l. and a constant speed of 13 m/s. Survey/tie lines were respectively flown roughly parallel/perpendicular to the coast at a 10/80 m spacing. Diurnal variations of the magnetic field were corrected for using data of a GSM-19 base station continuously recorded in the vicinity of the survey area. Detailed survey parameters and processing are reported in [26]. The high-resolution UAV magnetic anomaly map is presented in Figure 4.

2.2.3. Petrophysics

In order to constrain the magnetic interpretation and modeling, κ (magnetic susceptibility) measurements were taken in the field using a SM-30 handheld kappameter. All lithologies outcropping in the study area were sampled: the facies of two granites and aplite-pegmatite veins, two gneisses, 3 different dolerite families, and the pseudo-skarn mineralization. In each facies, at least 5 sites were sampled (with several measurements in each site), in order to achieve representative statistics for each lithology. The location of kappameter measurements is provided in Figure 4, and Table 1 summarizes the magnetic susceptibility characteristics of each lithology.

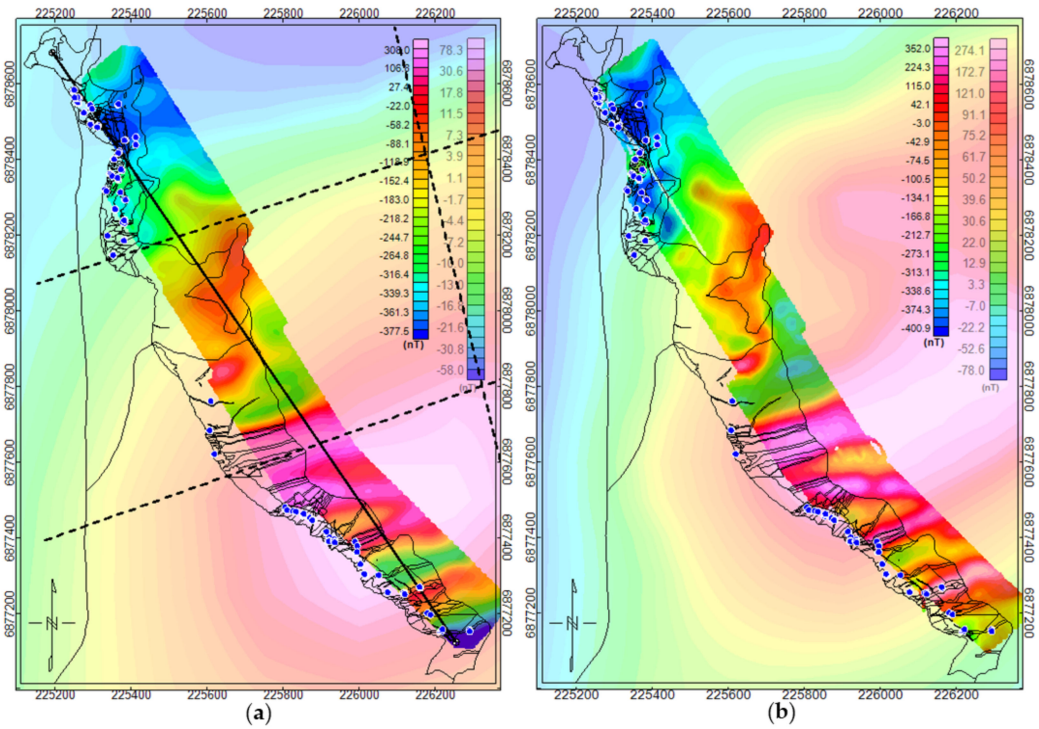

Figure 4. Magnetic map of the study area: (**a**) the magnetic anomaly on the left and (**b**) the anomaly reduced to the pole, on the right. Pale colors refer to the regional aeromagnetic map and bright colors, to the local drone-borne magnetic survey. Geological contours are superimposed in black and dark blue dots localize field magnetic susceptibility measurements. Location of modelled magnetic profiles represented as thick black dotted lines; the profile along the coast is presented in the following figures.

Table 1. Statistics of magnetic susceptibility measurements performed on each geological facies outcropping in the study area. A factor of 10^{-3} applies for SI units. In the Lithology descriptions, Bt and Hbl stand for biotite and hornblende respectively.

Aver.	Std.	# Sites	Code	Lithology
7.6	8.7	23	GPGN	Paleoproterozoic Bt-bearing grey paragneiss.
6.1	4.8	5	PMGT	Carboniferous Ploumanac'h monzogranite
7.1	4.6	6	PAPD	Carboniferous aplite-pegmatite dyke.
7.6	5.4	8	DPGN	Paleoproterozoic. Dark Bt+-Hbl-bearing gneiss
13.2	5.4	20	NSGT	Perros-Guirec Neoproterozoic meta-syenogranite.
32.8	39.6	22	DOL	Dolerite dyke
301.2	288.2	13	SK	Pseudoskarn accompanying dolerites, granites and gneisses
25.7	20.2	5	DOLA	1st gen. of mafic dykes including numerous fine grained mafic enclaves
0.4	0.3	6	DOLF	2nd gen. of mafic dyke. Strongly foliated mafic dyke.

In addition, to Table 1, it must be noted that on pseudo-skarn outcrops, often the kappameter readings exceeded the measurement range of the device (i.e., higher than 999×10^{-3} SI). Actually, native macroscopic magnetite was the usual constituent on pseudo-skarn outcrops: it was visually evaluated that the mineralization deposit was constituted of 50% of magnetite on average, locally close to 100%. After [27], an empiric log-log relationship links the magnetite content of rocks and their magnetic susceptibility, which shows that for 100% of magnetite, $\kappa > 10$ SI, and is around 5 SI for 50% magnetite. We actually used this value of 5 SI for modeling the pseudo-skarn. It is also probable that the pseudo-skarn mineralization is partly remanent. But this component of rock magnetization was not measured, and we didn't consider it, since there was no obvious evidence of predominant remanence in the study area: actually, the magnetic map reduced to the pole does not display obvious dipolar anomalies (Figure 4), which means that magnetization in the rocks involved in the area is predominantly induced.

3. Results

3.1. Field-UAV Detailed Geological Mapping

The study area is along the shore, at the foot of the cliff, accessible at low tide only (tide vertical amplitude reached 20 m during the survey); it consists of small to large boulders partly covered by algae, making the beach extremely difficult to survey on foot (Figure 1). The entire area (approximately 2 km long and 150 m wide, at low tide) was surveyed for detailed geology in approximately five days, totalizing more than 100 observation sites. These observations were interpreted in relation to the 1:50,000 geological map, and detailed geological contours and structures were drawn in a GIS at the 1:500 scale, with the help of the multispectral mosaic (see example in Figure 3). A resume of the detailed geology mapped on the shore is provided hereafter, which will support the geophysical modeling.

The Paleo-Proterozoic gneisses are represented by various types of gneisses that crop between the Variscan Ploumanac'h granite and the Cadomian Perros-Guirec granite (Figure 2). These layered gneisses are probable volcano-sedimentary metasediments composed of plagioclase, quartz, K-feldspar, and biotite. They are locally intruded by porphyric orthogneiss. Locally, these gneisses are strongly mylonitized and brecciated by SW-NE-trending faults. The metamorphic foliation trends on average at N160° E/65° SW. These gneisses are transformed into cordierite-bearing hornfels along the contact with the Variscan Ploumanac'h intrusion and are crosscut by a swarm of aplite-pegmatite dyke associated with this intrusion (Figure 5). In the vicinity of the Cadomian Perros-Guirec granite, the Paleo-Proterozoic gneisses are injected by several intrusions of fine-grained Perros-Guirec granite and pegmatite-aplite dykes, and masses associated with this granite. The fine to middle-grained Perros-Guirec monzogranite is composed of 3–5 mm ovoid quartz, plagioclase, biotite, K-feldspar, and locally some muscovite. The western border of this granite is deformed by ductile and brittle deformation. Both the Paleo-Proterozoic gneisses and the Cadomian Perros-Guirec granite are crosscut by three generations of mafic dykes (Figures 3 and 5). The first generation is subvertical, it trends N60 to N45° E. Low-angle reverse faults crosscut this first generation of dykes, they trend N130° E within the Perros-Guirec granite, to N170° E in the gneiss, with an average dip of 35° to the west. These faults are filled by the second generation of strongly weathered phlogopite-bearing mafic material. The third generation of dolerite dykes crosscuts both previous dyke generations. Mafic dykes are transformed into amphibolites close to the contact with the Variscan Ploumanac'h granite. A swarm of pegmatite aplite dykes associated with the Ploumanac'h granite crosscuts almost vertically all the previous lithologies along an N70 to N130° E trend. Disseminated magnetite is found in some of these pegmatites as well as in the Ploumanac'h granite itself (Figure 5). Locally, numerous decametric to pluri-metric outcrops of a skarn-like assemblage composed of magnetite, garnet, epidote, quartz, albite, pyrite, scheelite, and molybdenite, develops along the contacts between the first and the second generation of mafic dykes and the Perros-Guirec granite (Figure 5). In several well-exposed areas, this pseudo-skarn is composed of 50% volume magnetite, or even more.

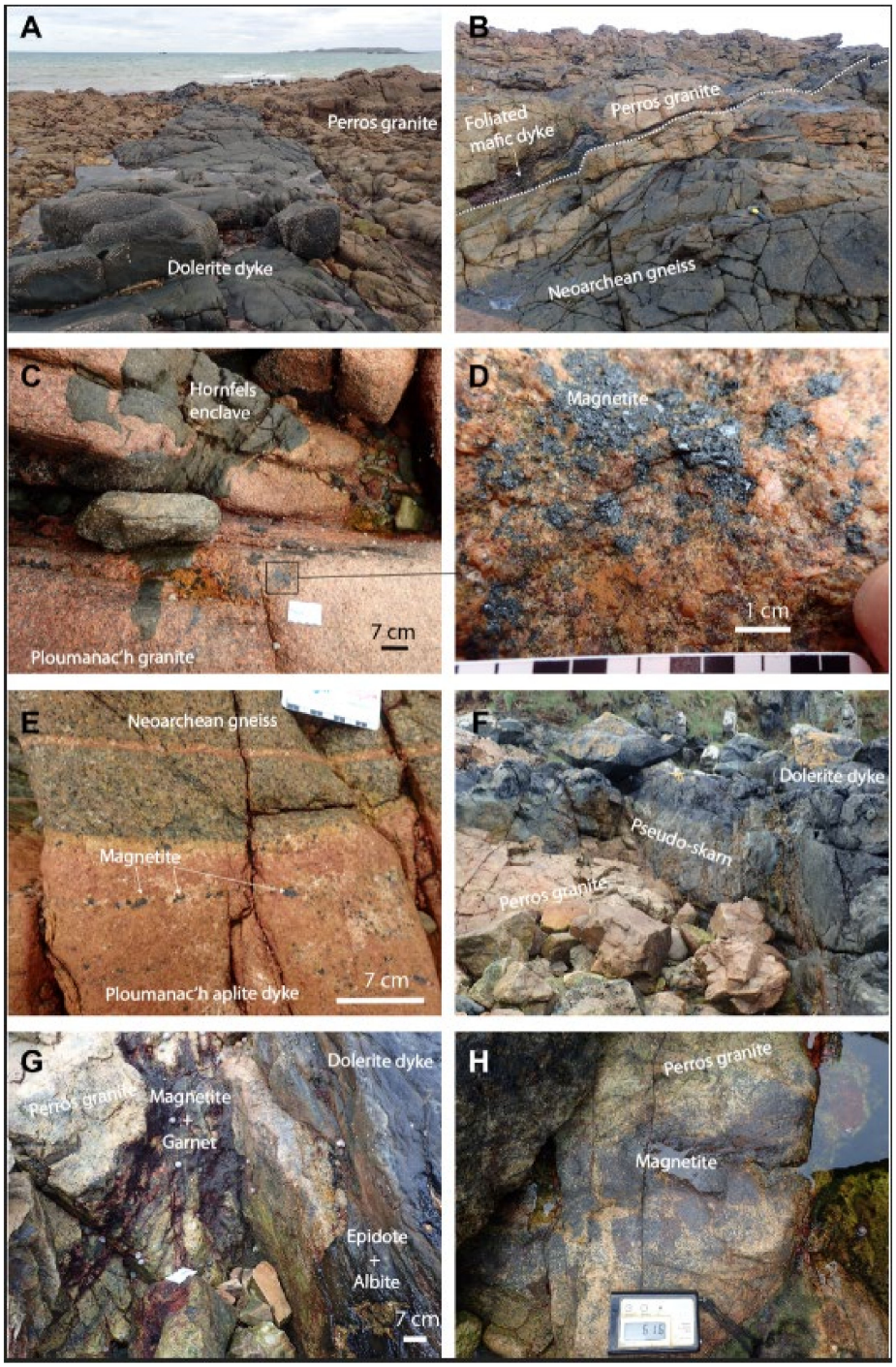

Figure 5. Selected images illustrating the relationships between the pseudo-skarn and the Carboniferous magmatism and associated late magmatic and hydrothermal fluids. (**A**) NE-SW-trending 3 m-thick mafic dyke crosscutting the Neoproterozoic Perros-Guirec granite. (**B**) Strongly deformed mafic dyke of the second generation injected within a low dipping reverse fault. Fault dip is to the west. (**C**,**D**) Disseminated magnetite within Ploumanac'h Carboniferous monzogranite, close to the border of the intrusion. (**E**) Disseminated magnetite within a Ploumanac'h aplite dyke crosscutting the Paleo-Proterozoic gneiss. (**F**) Pseudo-skarn (light green) at the contact between a first generation of dolerite dyke and the Neoproterozoic Perros-Guirec granite. (**G**) Close view of the pseudo-skarn along the contact between a dolerite dyke and Perros-Guirec granite. Numerous veins mainly composed of epidote+albite are located in the dolerite and numerous dissemination of mainly magnetite+garnet are located within the Perros-Guirec granite. (**H**) Example of massive magnetite disseminated within Perros-Guirec granite. Kappameter for scale with a magnetic susceptibility measurement of 616×10^{-3} SI.

3.2. Magnetic Modelling

Based on the detailed geological map and structural information gathered in the field, as well as the petrophysical constraints, forward magnetic modeling was performed along four profiles (location in Figure 4a). Modeling along four crossing profiles allowed strengthening the overall geometries; in the following, only the profile along the coast is presented since it is best constrained by ground observations, and it is the only one fully covered by the magnetic UAV survey. The magnetic modeling is performed first, using the regional fixed wing aeromagnetic data, then focusing on the detailed UAV-borne survey.

3.2.1. Regional Magnetic Modelling

First, magnetic modeling was performed at the regional scale in order to position the main geological units with respect to the regional geological map, evaluate their "background" magnetic effect, given their petrophysical characteristics, and finally, sketch the pseudo-skarn overall geometry, by fitting the large prominent magnetic anomaly. Because the magnetic susceptibility of the pseudo-skarn is very high, its geometry revealed extremely sensitive on the modeling. Since pseudo-skarn masses are systematically developed along permeable structures, i.e., along dolerite dykes and within fractures and faults, it was considered that the mineralization would not exceed a few tens of centimeters in thickness (it was modeled as a ±35 cm thick ribbon) at the contact with a dolerite dyke, which thickness was set to an average of two meters (again, based on field observations). Actually, the pseudo-skarn mineralization results from the circulation of Fe-Mg rich fluids deriving from Ploumanac'h batholith along the dolerite dykes, and reacting with their calcium content [12]. The very sensitive modeling of the "skarn-dolerite ribbon" suggests that a very simple sill-shaped, slightly concave geometry, at shallow depths (ranging between 10 and 150 m), can account for the regional magnetic anomaly (Figure 6). This geometry is compatible with the second generation of mafic dykes intruded along low-dipping faults. Fine-tuning of this geometry was cross-constrained between the four profiles modeled regionally (location in Figure 4a), which gives rather good confidence on it, at this scale.

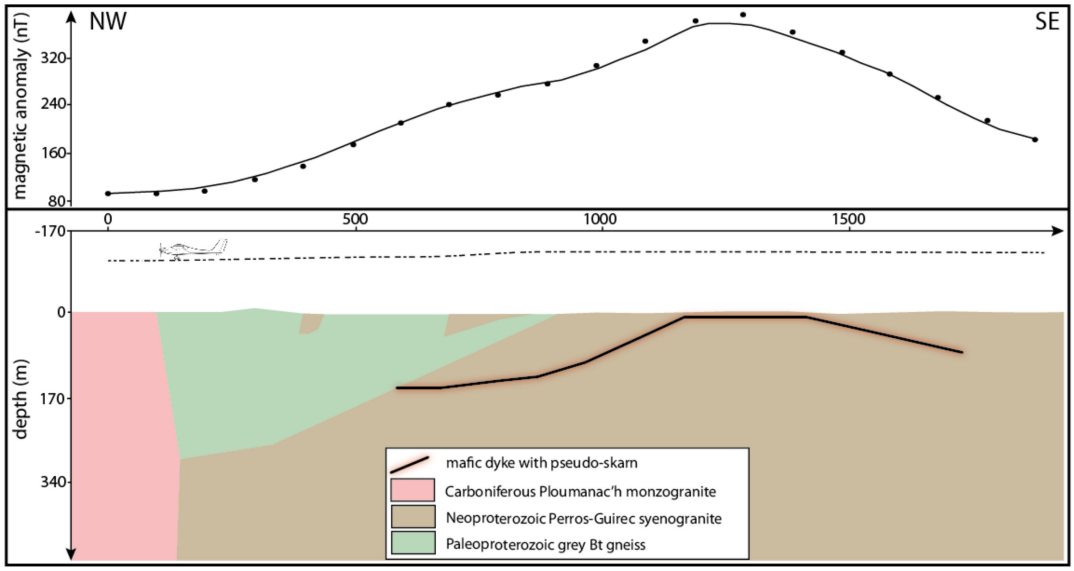

Figure 6. Regional magnetic modelling along the coast (profile location on Figure 4a). Upper window: measured regional magnetic anomaly (dots) compared to the computed magnetic model effect (line). Lower window: colors of modelled geological units are consistent with Figure 2. Taking into account a realistic "geological magnetic background", a good fit of the regional magnetic anomaly can be achieved with a "ribbon-shaped" pseudo-skarn developed along a low-dipping mafic dyke (in black with red shadow—exaggerated in thickness). Vertical exaggeration is 1 for all displayed cross-sections.

3.2.2. From Regional to Local Magnetic Modeling

Second, the geometry modeled at the regional scale was transferred to the local scale (for the profile running along the coast, within the UAV survey area) and confronted with the high-resolution magnetic data (Figure 7). To the first order, the overall fit of the computed/measured magnetic anomaly is rather good; only slight modifications of the pseudo-skarn low-dipping mafic dyke were introduced to fit the central low magnetic anomaly. Southeast of the profile, the short wavelength anomalies are not fitted by this regional model: in the next step, it is investigated if these anomalies can be accounted for introducing the dolerite dykes cross-cutting Perros-Guirec granite, mapped in the field.

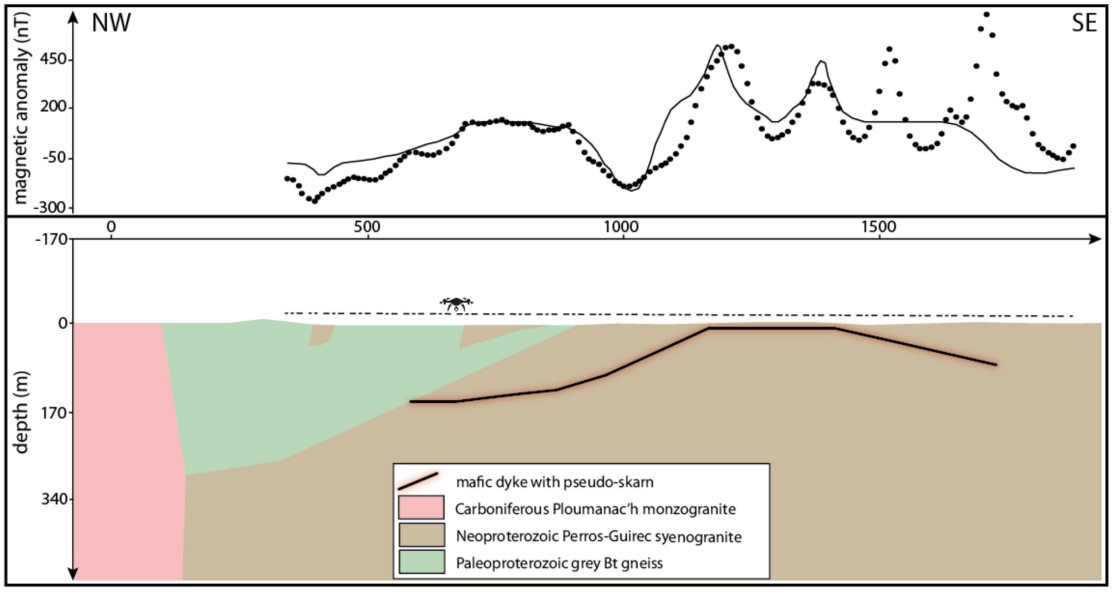

Figure 7. Regional magnetic model along the coast, confronted with the high-resolution UAV magnetic data. Upper window: UAV-borne measured magnetic anomaly (dots) compared to the computed magnetic model effect (line). Lower window: colors of modelled geological units are consistent with Figure 2. The overall fit of the profile is surprisingly good, most magnetic anomalies are fitted at the first order, except short wavelength anomalies at the southeastern end of the profile.

3.2.3. Local Model Refinement: Geophysically Driven

Third step: the very good cartographic fit between most of the mapped dykes and the linear magnetic anomalies mapped in the UAV survey (Figures 3 and 4) argues in favor of the dolerites being the source of these anomalies. Accordingly, taking into account the position of the first and third generations of subvertical outcropping dykes and their actual measured susceptibilities, the short wavelength magnetic anomalies were fitted (Figure 8). In order to achieve a proper magnetic fit, dykes were considered anastomosed at depth, which allows increasing and widening the magnetic effect of each separate dyke.

3.2.4. Final Geologically Constrained Model

Last modeling step: According to the geological field observation and magmatism concepts, the dolerite dykes outcropping in the southeastern end of the study area were presumably emplaced as pseudo-2D sheets, extending both on large horizontal distances, at the regional scale (these dykes are mapped throughout northern Brittany (e.g., [28]), and also extending subvertically at great depth, rather than anastomosed, such as previously "geophysically modeled". In the modeling, however, the vertical dyke sheets alone, cannot account for the entire magnetic signal as shown in Figure 9 (their magnetic effect, displayed in grey in the upper panel of the figure, does not fully fit the observed data points). Therefore, as suggested by field observation of discontinuous skarn mineralization along some of the outcropping dolerite dykes (and attested by field kappameter measurements), it was considered that mineralizing fluids drained along the low-dipping mafic dyke could

have been channeled along some of the vertical dykes and could have induced skarn mineralization along them, over vertical distances of meters to tens of meters. This is what the model of Figure 9 depicts, allowing for a good fit of the magnetic data.

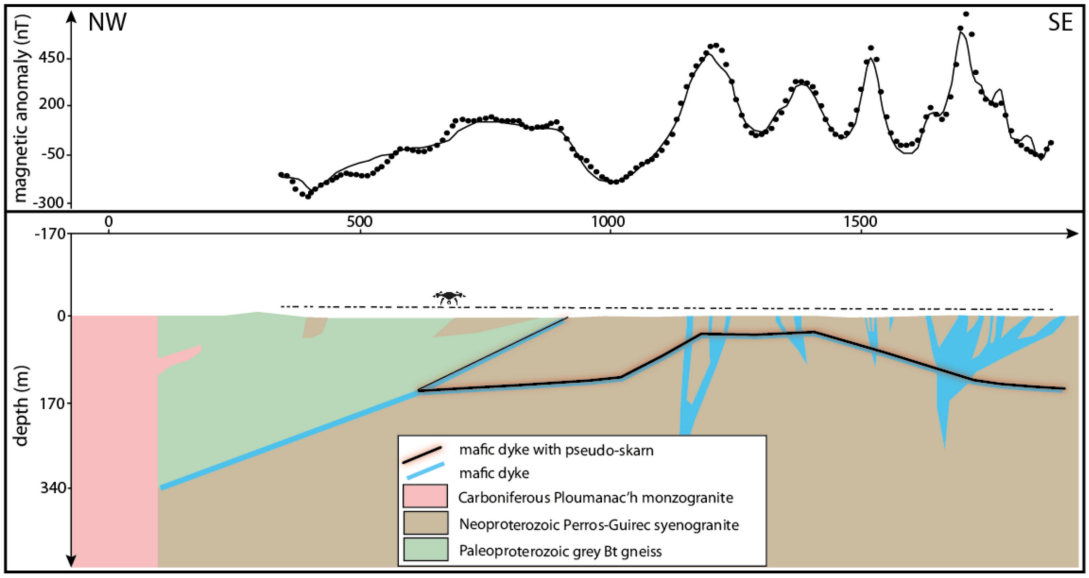

Figure 8. Local magnetic model along the coast: outcropping dykes and their actual measured magnetic susceptibility, as well as an ad hoc anastomosis at depth allow fitting the high resolution magnetic data. Upper window: UAV-borne measured magnetic anomaly (dots) compared to the computed magnetic model effect (line). Lower window: colors of modelled geological units are consistent with Figure 2.

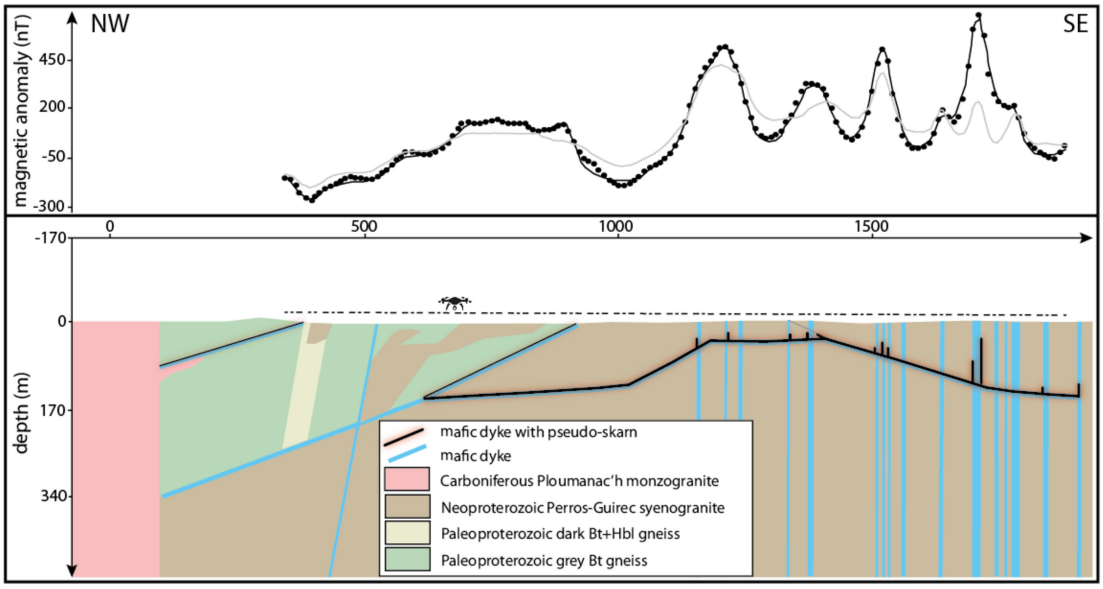

Figure 9. Final magnetic model along the coast. Upper window: UAV-borne measured magnetic anomaly (dots) compared to the computed magnetic model effect (line). Lower window: colors of modelled geological units are consistent with Figure 2. 1st and 3rd dolerite dyke generations are modelled as 2D subvertical sheets; their magnetic effect only cannot account for the entire magnetic signal (grey line in upper panel). For the final fit of the magnetic data (black line in upper panel), pseudo-skarn mineralization (in black with red shadow—exaggerated in size) was modelled channeled along some of the vertical dolerite dykes, in connection with the mineralized 2nd generation low-dipping mafic dyke.

3.3. 3D Geological Modelling

In order to evaluate the 3D consistency of the 2D model of the mineralization with available geological and structural observations, it was integrated in a 3D geometrical model within 3D-Geomodeller© software [29]. The 3D model was generated taking into account data available on two surfaces: 1—field observations and structural dips on the topography and 2—geological contacts in the modeled cross-section. The 3D interpolation process in 3D-Geomodeller© produces 3D surfaces shaped by the available dip measurements and which honor the contact points. This process consistently takes into account all contact/dip data provided in all cross sections.

A subset of the 3D model is displayed in Figure 10: the upper low-dipping mafic dyke geometry, based on field observations, takes into account a constant dip of 35° to the west and the gradual change in orientation of the structure from the NW to the SE of the beach. It, therefore, appears as a slightly concave "sheet" gently dipping to the west. The arcuate shape of the main mineralized structure in the magnetic model (Figure 9) is apparent: it is the result of the intersection of the straight geophysical cross-section with the convex shape of the structure along the beach. Therefore, in 3D, the model of the main mineralized structure (lower low-dipping mafic dyke), derived from the magnetic modeling, also appears as a slightly concave "sheet" dipping towards the west. Finally, these two structures, derived from completely different data sources, display consistent subparallel geometries.

As evidenced in our magnetic modeling, the skarnified low-dipping mafic dyke, which produces most of the magnetic anomaly does not outcrop. However, what could be interpreted as a minor replica of this main mineralized low-dipping mafic dyke outcrops discontinuously with a consistent trend all along the beach (in Figure 2, faults mapped, sub-parallel to the coast from the SE to the NW of the study area). In the field, this structure is materialized from place to place by strongly altered phlogopite-bearing mafic dykes intruded in a low-angle reverse fault. These faults/dykes trend N130° E in the east, within the Perros-Guirec granite, to N170° E in the Paleo-Proterozoic gneiss. Their dip is on average 35° to the west. Our magnetic modeling connects this low angle structure to Ploumanac'h batholith some tens of meters below the surface (left of cross-section, Figure 9). As also suggested left of Figure 9, Ploumanac'h granite might be injected along these low angle reverse faults; indeed, flat angle patches of granite are observed outcropping within the gneisses. Observations and understanding of this structuration, and associated magmatism and dyke emplacement are tentatively transferred to the main mineralized structure modeled at depth. This structure, modeled, based on magnetic constraints, is interpreted as mafic material (and possibly also granitic material) injected into an inverse low angle reverse fault, probably formed during an early stage of Ploumanac'h batholith emplacement. In the last stages of cooling of the batholith, Fe-Mg-Mo-W rich fluids circulated along these pre-existing structures transforming dolerite and granite into a Fe-Mo-W skarn-like assemblage. Field observations and our magnetic modeling also suggest that the fluids are also channeled towards the surface along subvertical older dykes. Our modeling suggests that this occurs where the vertical dykes are cross-cut by the low angle main mineralized structure. Further dating of the three generations of subvertical dykes, of the reverse low angle fault and the material injected in it, as well as of the mineralization would be needed to ascertain this tentative model.

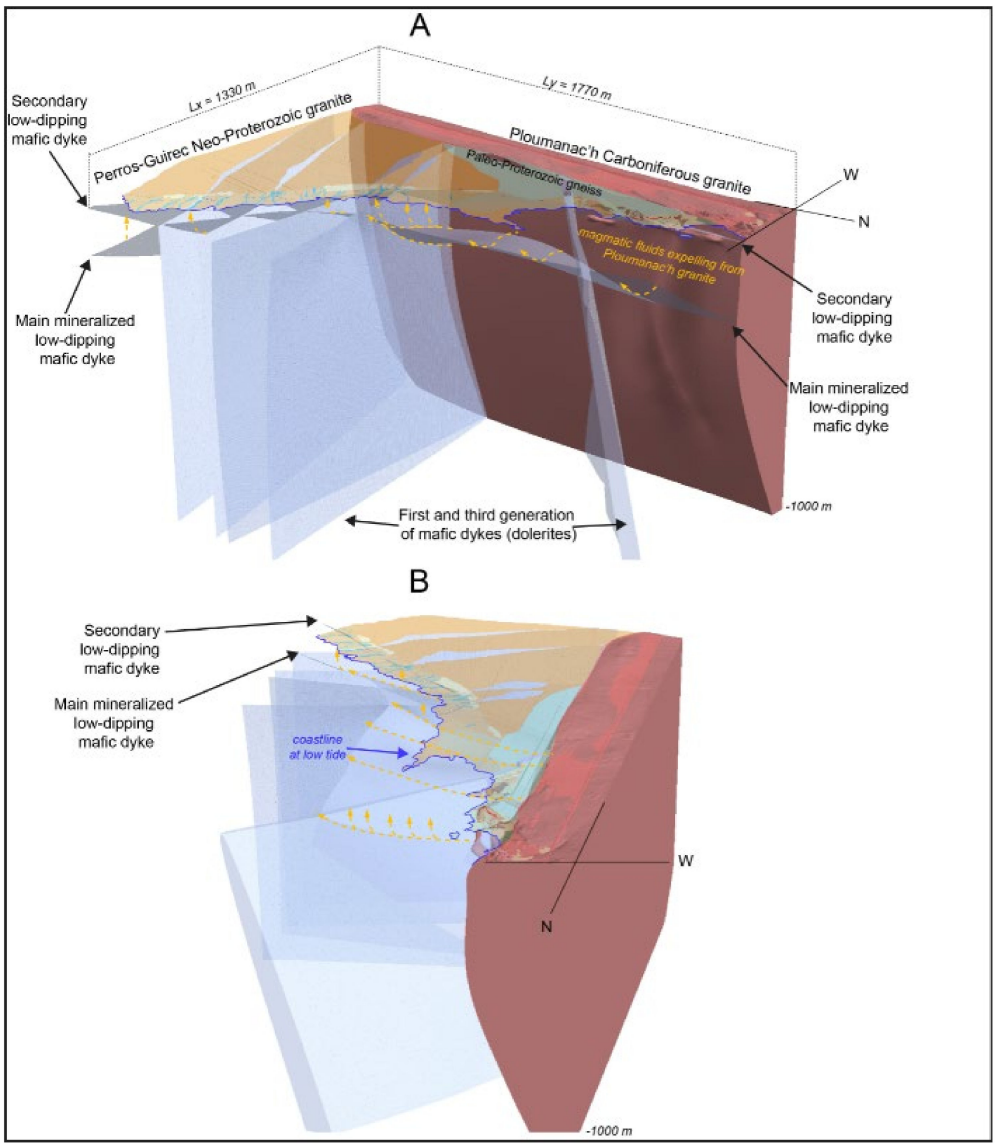

Figure 10. Two views (A from NE and B from NNW) of the3D geometrical model of the study area (1330 m × 1770 m × 1000 m), focused on the dykes channeling the mineralizing fluids (yellow arrows) as a result of Ploumanc'h granite cooling. 3D model created in Geomodeller© 4.0.7 software viewed and annoted in ESRI ArcScene© 10.5.1. For clarity, the Perros-Guirec granite and the Paleo-Proterozoic gneiss have been removed at depth from the 3D view but are still visible on the surface geology limited by the coastline at low tide (blue line). Also, only some of the main mafic dykes are represented. The main mineralized low-dipping mafic dyke does not crop, its geometry derives from the magnetic modelling. The secondary more superficial low-dipping mafic dyke, outcrops along the coast, it dips westwards rather constantly at 35°, with an orientation slightly rotating between N130° E and N170° E from south to north. The detailed 3D modelling of both low-dipping dykes, taking into account field measurement and the magnetic model geometry at depth, clearly shows that both structures are subparallel. Therefore, the slightly mineralized low-dipping mafic dyke outcropping along the beach, emplaced in a low-angle reverse fault, is a nice accessible replica of the main mineralized structure at depth.

4. Discussion

It is well known that potential field models are non-unique. However, in magnetic modeling, when magnetic properties of rocks are contrasted (such as with skarn-magnetite mineralization), the modeling is extremely sensitive to very small modifications of the geometry (and magnetic properties). Therefore, introducing a few constraints of geometry such as the geological outcrops and dips and taking few assumptions such as keeping a constant mineralization thickness (which looks realistic to the first order in the process

of channeling fluids along dolerite dykes), the degrees of freedom of the modeling are drastically reduced. Even the average depth of the mineralized structure is fairly well constrained: the combination of the very high magnetization contrast and the constant thickness of the mineralized layer allows very little variation in depth/geometry to fit the measured anomaly. And this constraint is even stronger when this geometry must fit both the regional and the detailed magnetic data. However, the model does not intend to perfectly match the geological reality, because 1—the mineralized structure is certainly not perfectly continuous and with a perfect constant thickness (considered to be $\pm$35 cm in our modeling), 2—as evidenced by magnetic susceptibility data in the field, its magnetization is also not perfectly constant (considered to be 5 SI in our modeling) and it is also probably partly remnant, despite no evidence after reduction to the pole. In addition to forward modeling, it has been tested to "strengthen" the magnetic model through 3D inversion, within its geological environment, using the stochastic process implemented in 3DGeomodeller. But the results were either not computationally feasible (because the thin mineralized layer requires very thin meshing and therefore tenfolds computation time), or, if the mesh is downgraded, inversion results unrealistically "spray" the mineralization zone and do not display significant discrepancy with the forward modeling geometry, or provide new understanding of the system.

The ability of drone data to bridge the gap between field observations/measurements and regional geophysical data is easily understandable. It is demonstrated in this study 1—by the combination of multispectral imagery with field geological observations in order to enhance the detailed geological mapping, and 2—by the combination of field magnetic susceptibility measurement and their use in detailed to regional magnetic modeling constrained respectively by drone-borne and airborne magnetic surveys. Another less obvious but outstandingly important aspect of this multiscale approach, especially in mineral prospection, occurs during the modeling phase. In our case study—and presumably, in every geophysical mineral targeting work—the combination of the drone and regional magnetic data allowed us to derive a geological/mineralization model of better reliability than with work at one scale only: 1—with high resolution focused drone data only, it is most probable that the mineralized low-dipping mafic dyke at depth would not have been intuited because, at first sight, the magnetic drone map suggests that the E-W trending dyke swarm holds the magnetization, 2—with the regional magnetic anomaly only, the detailed structure of the mineralization channelized by the low-dipping mafic dyke at depth and locally connected to the surface along the subvertical older cross-cutting dyke swarm, could not be constrained.

5. Conclusions

UAV geophysical surveying is changing fast, providing increasingly diversified and fast access to high-resolution surface and subsurface information to a variety of stakeholders. The ability of drones to quickly map small to intermediate areas, bridging the gap between local field observations and regional airborne geophysical surveys has been addressed by several publications. We emphasize this aspect, more specifically regarding the link which can be made between field observations/measurements and the 3D modeling of the geology constrained by surface multispectral imagery (for accurate geological mapping), and magnetic data (to constrain subsurface geometries). This is demonstrated in a case study in a complex polyphased magmatic-metamorphic environment on the coast of French Brittany. The target area hosts a pseudo-skarn mineralization, exhibiting an outstanding magnetic anomaly.

The multiscale magnetic modeling performed against regional airborne data as well as local detailed UAV-borne data, tightly constrained by field geological observations, allows deriving a consistent and realistic magnetic description of the pseudo-skarn mineralization in its geological environment. It is stressed that most probably, if the magnetic modeling had been performed either at the local scale only (with high-resolution drone data) or the regional scale only (with airborne data), the geometrical as well as conceptual geological

and mineralizing model could not have been realistically depicted, in such compliance with field geological observations. The final 3D integration of surface geological observations with subsurface modeled geometries confirms the overall geometrical consistency of the main deep mineralized structure with a secondary replica observed in the field.

Author Contributions: Conceptualization, G.M., E.G., A.D. and T.M.R.; methodology, G.M., E.G. and A.D.; fieldwork, E.L.S.d.S., A.D., E.G., J.L., G.M. and T.M.R.; writing—original draft preparation, G.M., E.G.; writing—review and editing, A.D., T.M.R., E.G., G.M. and E.L.S.d.S.; project administration, A.D., funding acquisition, A.D., G.M. and T.M.R. All authors have read and agreed to the published version of the manuscript.

Funding: This research was funded by EIT-RM (https://eitrawmaterials.eu/project/muverdrone/, accessed on 10 November 2021).

Data Availability Statement: The data presented in this study are available on request from the corresponding author.

Acknowledgments: We thank the municipalities of Ploumanac'h and Perros Guirec as well as the Maison du littoral who facilitated the access to the field study area. We appreciate and thank three reviewers and Minerals Associate editor for their comments, which helped improve the manuscript.

Conflicts of Interest: The authors declare no conflict of interest. The funders had no role in the design of the study; in the collection, analyses, or interpretation of data; in the writing of the manuscript, or in the decision to publish the results.

References

1. Aleshin, I.M.; Ivanov, S.D.; Koryagin, V.N.; Matveev, M.A.; Morozov, Y.A.; Perederin, F.V.; Kholodkov, K.I. Review on the use of light unmanned aerial vehicles in geological and geophysical research. *Seism. Instrum.* **2020**, *56*, 509–515. [CrossRef]
2. Heincke, B.; Jackisch, R.; Saartenoja, A.; Salmirinne, H.; Rapp, S.; Zimmermann, R.; Pirttijärvi, M.; Sörensen, E.V.; Gloaguen, R.; Ek, L.; et al. Developing multi-sensor drones for geological mapping and mineral exploration: Setup and first results from the MULSEDRO project. *GEUS Bull.* **2019**, *43*. [CrossRef]
3. Kim, B. Aeromagnetic exploration using unmanned aerial vehicles: Current and future trends. *Geophys. Geophys. Explor.* **2020**, *23*, 178–191.
4. Parshin, A.; Bashkeev, A.; Davidenko, Y.; Persova, M.; Iakovlev, S.; Bukhalov, S.; Grebenkin, N.; Tokareva, M. Lightweight unmanned aerial system for time-domain electromagnetic prospecting—the next stage in applied UAV-Geophysics. *Appl. Sci.* **2021**, *11*, 2060. [CrossRef]
5. Middlemiss, R.P. A Practical MEMS Gravimeter. Ph.D. Thesis, University of Glasgow, Glasgow, UK, 2016.
6. Limburg, H.; van der Veeke, S.; Koomans, R. Towards drone-borne gammaray mapping of soils. *First Break* **2019**, *37*, 55–61. [CrossRef]
7. Jansen, J.; Bell, R. *Drone Based Geophysical Surveys for Groundwater Applications*; Groundwater Week; US National Ground Water Association: Westerville, OH, USA, 2019.
8. Valentine, S. Geophysical trespass, privacy, and drones in oil and gas exploration. *J. Air Law Commer.* **2019**, *84*, 507.
9. Colorado, J.; Perez, M.; Mondragon, I.; Mendez, D.; Parra, C.; Devia, C.; Martinez-Moritz, J.; Neira, L. An integrated aerial system for landmine detection: SDR-based Ground Penetrating Radar onboard an autonomous drone. *Adv. Robot.* **2017**, *31*, 791–808. [CrossRef]
10. Park, S.; Choi, Y. Applications of unmanned aerial vehicles in mining from exploration to reclamation: A review. *Minerals* **2020**, *10*, 663. [CrossRef]
11. Le Maire, P.; Bertrand, L.; Munschy, M.; Diraison, M.; Géraud, Y. Aerial magnetic mapping with an unmanned aerial vehicle and a fluxgate magnetometer: A new method for rapid mapping and upscaling from the field to regional scale. *Geophys. Prosp.* **2020**, *68*, 2307–2319. [CrossRef]
12. Chauris, L. Un pseudo-skarn fissural à molybdénite et scheelite: Kerdu en Perros-Guirec (*Massif armoricain*). *Bull. Soc. Sci. Nat. Ouest Fr.* **1991**, *13*, 41–50.
13. Egal, E.; Guerrot, C.; Thiéblemont, D.; Chantraine, J. The Cadomian Orogeny revisited in northern Britanny (France). In *Avalonian and Related Peri-Gwondanan Terraces of the Circum-North Atlantic*; Nance, R.-D., Thompson, M.-D., Eds.; The Geological Society: London, UK, 1996; Volume 304, pp. 281–318.
14. Graviou, P. Pétrogenèse des Magmas Calco-Alcalins: Exemple des Granitoïdes Cadomiens de la Région Trégorroise (Massif Armoricain). Ph.D. Thesis, Université de Rennes, Rennes, France, 1984; 236p.
15. Thiéblemont, D.; Egal, E.; Chantraine, J. Révision du volcanisme cadomien dans l'Est du Trégor (Bretagne nord). *Géol. Fr.* **1996**, *4*, 3–21.

16. Auvray, B. Genèse et Evolution de la Croûte Continentale dans le Nord du Massif armoricain. Ph.D. Thesis, Rennes University, Rennes, France, 1979; 680p.
17. Barboni, M.; Schoene, B.; Ovtcharova, M.; Bussy, F.; Schaltegger, U.; Gerdes, A. Timing of incremental pluton construction and magmatic activity in a back-arc setting revealed by ID-TIMS U/Pb and Hf isotopes on complex zircon grains. *Chem. Geol.* **2013**, *342*, 76–93. [CrossRef]
18. Pochon, A.; Poujol, M.; Gloaguen, E.; Branquet, Y.; Cagnard, F.; Gumiaux, C.; Gapais, D. U-Pb LA-ICP-MS dating of apatite in mafic rocks: Evidence for a major magmatic event at the Devonian-Carboniferous boundary in the Armorican Massif (France). *Am. Miner.* **2016**, *101*, 2430–2442. [CrossRef]
19. Albarède, F.; Dupuis, C.; Taylor, H.-P., Jr. 18O/16O evidence for non-cogenetic magmas associated in a 300 Ma old concentric pluton at Ploumanac'h. *J. Geol. Soc.* **1980**, *137*, 641–647. [CrossRef]
20. Guennoc, P.; Feybesse, J.-L.; Hallégouët, B.; Lebret, P.; Chauris, L.; Lucassou, F.; Thiéblemont, D.; Choulet, F.; Eglinger, A.; Bourdillon, C.; et al. *Explanatory Note of the Geological Map of France 1:50,000 Scale, Perros Guirec Sheet (170)*; BRGM: Orléans, France, 2015; 264p.
21. Barrière, M. Le complexe de Ploumanac'h (Massif armoricain). Essai sur la Mise en Place et L'évolution Petrologique d'une Association Plutonique Sub-Alcaline Tardi-Orogénique. Ph.D. Thesis, UBO University, Brest, France, 1977; 291p.
22. Vigneresse, J.L.; Cuney, M.; Jolivet, J.; Bienfait, G. Selective heat-producing element enrichment in a crustal segment of the mid-European Variscan chain. *Tectonophysics* **1989**, *159*, 47–60. [CrossRef]
23. Chauris, L. Concentrations en terres rares et thorium dans les ségrégations biotitiques du granite rouge de Ploumanac'h (Massif armoricain). *Géol. Fr.* **1992**, *2*, 23–27.
24. Decitre, S.; Gasquet, D.; Marignac, C. Genesis of orbicular granitic rocks from the Ploumanac'h plutonic complex (Brittany, France): Petrolographical, mineralogical and geochemical constraints. *Eur. J. Miner.* **2002**, *14*, 715–731. [CrossRef]
25. Bonijoly, D.; Perrin, J.; Truffert, C.; Asfirane, F. *Couverture Géophysique Aéroportée du Massif armoricain, Magnétisme et Radiométrie Spectrale*; Rapport BRGM R 40471; BRGM: Paris, France, 1999; 75p.
26. Døssing, A.; Silva, E.L.S.D.; Martelet, G.; Rasmussen, T.M.; Gloaguen, E.; Petersen, J.T.; Linde, J. A high-speed, light-weight scalar magnetometer bird for km scale UAV magnetic surveying: On sensor choice, bird design, and quality of output data. *Remote Sens.* **2021**, *13*, 649. [CrossRef]
27. Grant, F.S.; West, G.F. *Interpretation Theory in Applied Geophysics*; McGraw-Hill Book: New York, NY, USA, 1965.
28. Oehler, J.F.; Lequentrec-Lalancette, M.F. The contribution of marine magnetics in the Gulf of Saint-Malo (Brittany, France) to the understanding of the geology of the North Armorican Cadomian belt. *C. R. Geosci.* **2019**, *351*, 1–9. [CrossRef]
29. Calcagno, P.; Chilès, J.P.; Courrioux, G.; Guillen, A. Geological modelling from field data and geological knowledge: Part, I. Modelling method coupling 3D potential-field interpolation and geological rules. *Phys. Earth Planet. Inter.* **2008**, *171*, 147–157. [CrossRef]